High Power Laser Science and Engineering, (2026), Vol. 14, e98, 10 pages.
doi:10.1017/hpl.2026.10200

HIGH POWER LASER SCIENCE AND ENGINEERING

RESEARCH ARTICLE

Experimental study of parametric-diffraction suppression via idler dissipation for multi-beam-pumped optical parametric amplification

Wentao Zhu[1], Yanfang Zhang[1], Peng Yuan[1,2], Zhipeng Qin[1,2], Jing Wang[2], Jingui Ma[1,2], and Liejia Qian[1,2,3]

[1] *Key Laboratory for Laser Plasma, School of Physics and Astronomy, Shanghai Jiao Tong University, Shanghai, China*

[2] *National Key Laboratory of Dark Matter Physics, School of Physics and Astronomy, Shanghai Jiao Tong University, Shanghai, China*

[3] *Tsung-Dao Lee Institute, Shanghai Jiao Tong University, Shanghai, China*

(Received 14 May 2026 UTC; revised 11 August 2026 UTC; accepted 10 September 2026 UTC)

Abstract

Multi-beam-pumped optical parametric chirped-pulse amplification (OPCPA) systems suffer from parasitic parametric diffraction caused by nonlinear cross-coupling among intense laser beams, which severely degrades conversion efficiency. Although quasi-parametric amplification has been proposed to suppress cascaded nonlinear effects, its quantitative effectiveness in mitigating multi-beam parametric diffraction has remained experimentally unexplored. In this work, we experimentally demonstrate a quasi-parametric chirped-pulse amplification (QPCPA) scheme that actively depletes idler waves in a Sm-doped yttrium calcium oxyborate crystal to suppress parametric diffraction. We characterize the dependence of parametric diffraction on the pump beam angle and intensity, and evaluate the suppression performance provided by idler dissipation. Experimental results in a two-beam-pumped configuration show that the QPCPA scheme reduces pump-to-diffraction conversion by more than 60% compared to conventional OPCPA. Robust cross-coupling suppression is maintained across a range of operating conditions. By establishing a clear experimental link between idler dissipation and diffraction suppression, this work provides a practical pathway for scalable energy enhancement in multi-beam nonlinear combining systems, supporting the advancement of high-energy OPCPA architectures.

Keywords: multi-beam-pumped amplification; nonlinear optics; optical parametric amplification; parametric diffraction

1. Introduction

Optical parametric chirped-pulse amplification (OPCPA) is a cornerstone technology for high-power femtosecond pulse generation, driving progress in attosecond science[1,2], laser-driven particle acceleration[3–5] and high-field physics[6–8]. However, energy scaling of OPCPA systems is fundamentally limited by the available pump energy in a single beam. To overcome this constraint, multi-beam pumping schemes have been developed to combine energy from multiple pump sources into a single signal beam via parametric gain[9–12]. An incoherent five-beam scheme has demonstrated experimental feasibility, achieving a pump-to-signal conversion efficiency exceeding 27%[13].

Beyond facilitating energy scaling, multi-beam pumping offers enhanced spectral control. For example, strategic two-beam pumping can amplify adjacent spectral regions[14,15]. Theoretical studies have predicted that wide-angle non-collinear OPCPA architectures may enable the generation of single-cycle petawatt-level pulses[16,17].

Despite these advantages, multi-beam-pumped OPCPA systems face a critical challenge from cascaded parasitic mixing processes. These are initiated by difference-frequency generation between idler waves and pump beams, followed by higher-order sum- and difference-frequency interactions[18–21]. Consider a two-beam pumping configuration: pump beams P_1 and P_2 amplify the primary signal S_0, generating corresponding idler waves I_1 and I_2. Subsequent parasitic nonlinear interactions, such as $P_1 - I_2 \rightarrow S_{12}$ and $P_2 - I_1 \rightarrow S_{21}$, generate secondary signal components S_{12} and S_{21}. These components are spectrally coincident with the original seed signal but propagate

Correspondence to: J. Wang, Key Laboratory for Laser Plasma, School of Physics and Astronomy, Shanghai Jiao Tong University, Shanghai 200240, China. Email: wangj1118@sjtu.edu.cn

© The Author(s), 2026. Published by Cambridge University Press in association with Chinese Laser Press. This is an Open Access article, distributed under the terms of the Creative Commons Attribution licence (https://creativecommons.org/licenses/by/4.0), which permits unrestricted re-use, distribution and reproduction, provided the original article is properly cited.

https://doi.org/10.1017/hpl.2026.10200 Published online by Cambridge University Press

along distinct angles determined by the noncollinear phase-matching conditions. This phenomenon, termed parametric diffraction, deflects a portion of the pump laser energy away from the intended beam path, thereby reducing conversion efficiency and degrading beam quality.

To address this limitation, we previously proposed a multi-beam-pumped quasi-parametric chirped-pulse amplification (QPCPA) scheme. Unlike conventional OPCPA, QPCPA actively dissipates the idler wave during the nonlinear amplification process[22]. Although idler dissipation slightly reduces the three-wave coupling strength and thus the signal gain relative to the ideal case, it significantly improves pump-to-signal conversion efficiency and renders the process insensitive to phase mismatch, supporting a large gain bandwidth[23,24]. Such spectral-selective idler dissipation can be implemented through multiple approaches, including rare-earth ion doping[23], frequency conversion[25–27] and spatial walk-off[28]. By suppressing idler-mediated energy transfer between adjacent pump channels at its source, QPCPA fundamentally prevents the cascade of parasitic processes, offering a more effective solution than methods relying solely on high seed injection[18–20].

In this work, we go beyond the previous theoretical proposal by providing the first experimental demonstration and quantitative characterization of parametric-diffraction suppression via QPCPA. Specifically, we elucidate the physical mechanisms underlying parametric diffraction through phase-matching analysis, and experimentally quantify its dependence on two critical scaling parameters – pump beam angular separation and pump intensity – which directly constrain the achievable energy in multi-beam-pumped systems. A direct comparative study between conventional two-beam-pumped OPCPA and QPCPA shows a reduction in pump-to-diffraction conversion exceeding 60%. These results establish a quantitative experimental link between controlled idler dissipation and parametric-diffraction suppression, providing validated guidelines for designing scalable, high-energy ultrafast laser systems based on nonlinear beam combining.

2. Theoretical analysis

2.1. Mechanism of parametric diffraction

Multi-beam-pumped OPCPA enables energy scaling by coherently transferring energy from multiple pump beams to a single signal via parametric amplification. This approach necessitates the precise optimization of the pump beam configuration to simultaneously satisfy noncollinear geometric constraints and the phase-matching conditions across all amplification channels.

For theoretical clarity, we utilize a two-beam-pumped system as a representative case. The dynamics of this system are modeled by extending the standard three-wave coupling equations under the slowly varying envelope approximation. The evolution for both conventional OPCPA (with idler dissipation coefficient $\alpha = 0$) and QPCPA ($\alpha \neq 0$) is governed by the following:

$$\frac{dA_s}{dz} = -i\kappa_s A_{p1} A_{i1}^* e^{-i\Delta k_1 z} - i\kappa_s A_{p2} A_{i2}^* e^{-i\Delta k_2 z}, \tag{1a}$$

$$\frac{dA_{p1}}{dz} = -i\kappa_{p1} A_s A_{i1} e^{i\Delta k_1 z}, \tag{1b}$$

$$\frac{dA_{p2}}{dz} = -i\kappa_{p2} A_s A_{i2} e^{i\Delta k_2 z}, \tag{1c}$$

$$\frac{dA_{i1}}{dz} = -i\kappa_{i1} A_{p1} A_s^* e^{-i\Delta k_1 z} - \frac{\alpha}{2} A_{i1}, \tag{1d}$$

$$\frac{dA_{i2}}{dz} = -i\kappa_{i2} A_{p2} A_s^* e^{-i\Delta k_2 z} - \frac{\alpha}{2} A_{i2}, \tag{1e}$$

where A_s, $A_{p1,2}$ and $A_{i1,2}$ represent the complex amplitudes of the signal (S_0), two pump beams (P_1 and P_2) and their corresponding idlers (I_1 and I_2), respectively. The nonlinear coupling coefficient is defined as $\kappa = \omega d_{eff}/nc$, where d_{eff} is the effective nonlinear coefficient, n is the refractive index, ω is the angular frequency and c is the speed of light in vacuum. The phase mismatch terms for the two parametric amplification channels are $\Delta k_1 = k_{p1} - k_s - k_{i1}$ and $\Delta k_2 = k_{p2} - k_s - k_{i2}$, respectively.

To account for first-order parametric diffraction ($P_1 - I_2 \rightarrow S_{12}$ and $P_2 - I_1 \rightarrow S_{21}$), we introduce two additional coupled-wave equations:

$$\frac{dA_{s12}}{dz} = -i\kappa_s A_{p1} A_{i2}^* e^{-i\Delta k_{12} z}, \tag{2a}$$

$$\frac{dA_{s21}}{dz} = -i\kappa_s A_{p2} A_{i1}^* e^{-i\Delta k_{21} z}, \tag{2b}$$

where A_{s12} and A_{s21} represent the complex amplitudes of the first-order diffracted signal. The phase mismatch terms of cross-coupling processes are defined as $\Delta k_{12} = k_{p1} - k_{s12} - k_{i2}$ and $\Delta k_{21} = k_{p2} - k_{s21} - k_{i1}$. In this analysis, the theoretical model is restricted to a two-beam-pumped geometry, and only first-order parametric diffraction is considered. This dual simplification isolates the primary cross-coupling channel and allows us to clearly identify and quantify the key physical relationships. Including higher-order processes would introduce additional idler absorption for multiple diffracted beams, complicating the direct attribution of suppression to the idler dissipation coefficient. As such, the first-order model provides the most transparent physical picture for the mechanism of interest. The experimentally observed higher-order diffraction is addressed separately via quantitative measurements.

This work employs a theoretical analysis based on published Sellmeier equations for yttrium calcium oxyborate (YCOB) crystals, selected for their suitability in QPCPA implementation via rare-earth doping to facilitate idler

https://doi.org/10.1017/hpl.2026.10200 Published online by Cambridge University Press

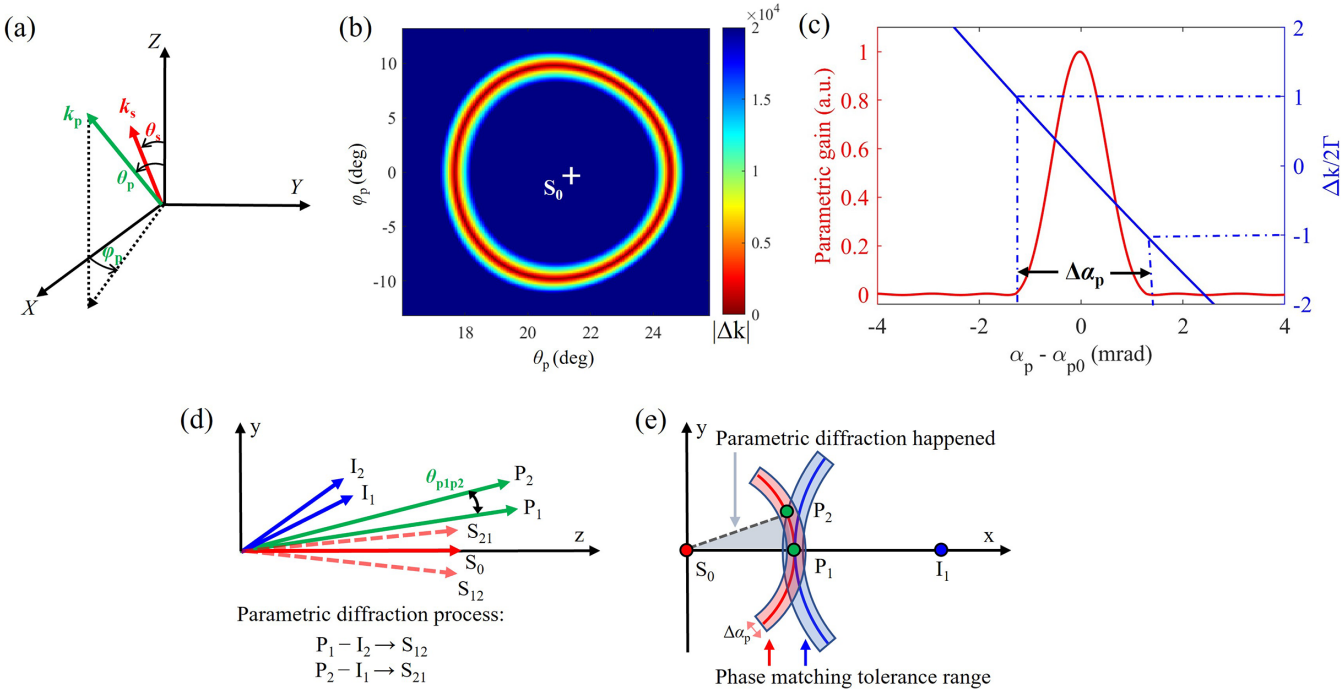


Figure 1. Phase-matching and parametric diffraction in two-beam-pumped OPCPA. (a) Angular relations in the dielectric frame (X, Y, Z). (b) Phase mismatch Δk versus pump incidence angles, showing the range of allowed pump directions. (c) Parametric gain (red curve) and normalized phase mismatch $\Delta k/2\Gamma$ (blue curve) as functions of noncollinear angle deviation. (d) Wave-mixing diagram in the z–y plane of the laboratory frame (x, y, z) illustrating parametric-diffraction processes $P_2 - I_1 \rightarrow S_{21}$ and $P_1 - I_2 \rightarrow S_{12}$. (e) Phase-matching tolerance analysis in the x–y plane of the laboratory frame (x, y, z): red and blue regions denote the angular tolerance ranges for the signal (S_0) and first idler (I_1), respectively. Parametric diffraction occurs when the second pump beam (P_2) lies within the overlap of these two tolerance cones.

absorption[23]. We consider a noncollinear Type-I phase-matching geometry with two pump beams. Figure 1(a) illustrates angular relations within the dielectric frame (X, Y, Z) for a 515 nm pump and an 800 nm signal. Broadband phase-matching is achieved at $\theta_p = 24.55°$ relative to the optic axis, with a noncollinear angle $\alpha_{p0} = 2.92°$ between the pump and signal. The signal propagates in the XZ plane ($\theta_s = 21.63°$, $\varphi_s = 0°$). Figure 1(b) displays the phase mismatch Δk as a function of pump incidence angles. Multiple pump beams can simultaneously satisfy phase-matching conditions with a single signal, forming a conical geometry of permissible pump directions (θ_p, φ_p) around the signal axis[29].

In practice, the angular tolerance $\Delta\alpha_p$ is defined as the permissible deviation of the pump wave vector from the optimal noncollinear angle α_{p0}. We quantify this tolerance by Taylor-expanding the phase mismatch Δk around α_{p0}:

$$\Delta k\left(\alpha_p\right) = \Delta k\left(\alpha_{p0}\right) + \left(\alpha_p - \alpha_{p0}\right)\frac{\partial \Delta k}{\partial \alpha_p} + \cdots . \tag{3}$$

In the small-signal regime (where pump depletion is negligible), the signal parametric gain follows $G \approx \exp(2gz)/4$, where the gain coefficient g is as follows:

$$g = \sqrt{\Gamma^2 - (\Delta k/2)^2}. \tag{4}$$

Here, Γ is nonlinear drive strength ($\Gamma^2 = 2\omega_s\omega_i d_{eff}^2 I_p / n_s n_i n_p \epsilon_0 c^3$)[30] and ϵ_0 is the permittivity of vacuum. Phase matching Δk dictates two distinct regimes. Here, $|\Delta k| < 2\Gamma$ yields exponential amplification, while $|\Delta k| > 2\Gamma$ results in oscillatory behavior without net gain. This transition at $|\Delta k| = 2\Gamma$ defines the angular tolerance $\Delta\alpha_p$ as follows:

$$\Delta\alpha_p = \frac{4\Gamma}{\frac{\partial \Delta k}{\partial \alpha_p}}. \tag{5}$$

Figure 1(c) presents the calculated parametric gain profile as a function of noncollinear angle deviation ($\alpha_p - \alpha_{p0}$) at a pump intensity of $I_p = 10$ GW/cm^2, a crystal length of $z = 3$ mm and $d_{eff} = 1.39$ pm/V. The gain spectrum exhibits peak gain at $\Delta\alpha_p = 0$ (perfect phase matching) and an angular tolerance of 2.6 mrad defined by $|\Delta k| = 2\Gamma$.

Building upon the angular tolerance analysis, we now examine parametric diffraction in a two-beam-pumped OPCPA system. The laboratory frame (x, y, z) is defined with the z-axis aligned along the signal wave vector. The first-order diffraction processes involve pump–idler cross-coupling ($P_1 - I_2 \rightarrow S_{12}$ and $P_2 - I_1 \rightarrow S_{21}$) in the laboratory frame, as shown in Figure 1(d). Here, θ_{p1p2} represents the angular separation between the two pump beams. Figure 1(e) illustrates the phase-matching geometry in the x–y plane of this frame. With S_0 and P_1 fixed, the idler I_1 is determined

https://doi.org/10.1017/hpl.2026.10200 Published online by Cambridge University Press

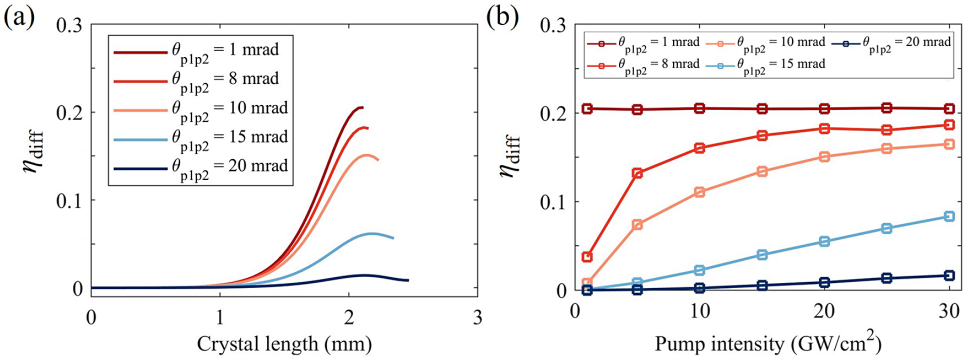


Figure 2. Numerical analysis of pump-to-diffraction conversion efficiency (η_{diff}) in a two-beam-pumped OPCPA system. (a) Calculated η_{diff} as a function of interaction length for different pump beam angular separations. (b) Calculated η_{diff} versus incident pump intensity.

by the phase matching. Parametric diffraction occurs when P_2 falls within the overlapping angular tolerance regions ($\Delta\alpha_p$) centered on S_0 and I_1, corresponding to the red and blue regions in Figure 1(e). This spatial overlap leads to undesired cross-coupling processes.

2.2. *Numerical simulation parameters and results*

We simulate a two-beam-pumped OPCPA system amplifying an 800 nm chirped signal pulse (2 ps duration, 150 nm full width at half maximum (FWHM) bandwidth) with two 515 nm pump beams (3 ps duration). To quantify parametric diffraction, we fix the position of P_1 and vary the angle of P_2 to maintain phase matching. Two efficiency metrics are defined: the pump-to-signal conversion efficiency η_s, and the parasitic pump-to-diffraction efficiency η_{diff}, which accounts for the first-order parasitic signals S_{12} and S_{21} as a direct energy loss mechanism. The simulations are performed with a single pump intensity I_p= 20 GW/cm^2 ($\Gamma = 1384$ m^{-1}) and a pump-to-signal intensity ratio $I_p/I_s = 10^3$. In the following two-beam-pumping configuration, the pump intensity refers to that of a single pump beam, and the two pump beams are assumed to have identical intensities.

As illustrated in Figure 2(a), η_{diff} reaches 20.5% at $\theta_{p1p2} = 1$ mrad, but decreases to 5.6% at $\theta_{p1p2} = 15$ mrad, demonstrating geometric control over parametric diffraction. For each configuration, the optimal crystal length is determined by maximizing the signal conversion efficiency η_s. A smaller pump angular separation increases the probability of cross-coupling, leading to accelerated pump depletion and a commensurate reduction in η_s.

Parametric diffraction also exhibits a characteristic pump-intensity scaling behavior, as shown in Figure 2(b). At large angular separations (e.g., $\theta_{p1p2} = 15$ mrad), the diffraction efficiency η_{diff} scales nearly linearly with pump intensity, rising from less than 0.1% at $I_p = 1$ GW/cm^2 to 8.3% at I_p = 30 GW/cm^2. This dependence reflects the $\Gamma^2 \propto I_p$ scaling of nonlinear coupling strength.

In contrast, at small angular separations (e.g., θ_{p1p2} = 1 mrad), η_{diff} saturates near 20%. This saturation originates from the coherent superposition of parametric interactions within the two-beam-pumping architecture. The signal complex amplitude A_s can be expressed as $A_s = A_{s1} + A_{s2}$, where A_{s1} and A_{s2} represent the complex amplitudes arising from interactions with P_1 and P_2, respectively. Under ideal conditions of small angular separation (perfect phase matching) and weak signal injection, the intrinsic amplification and the parametric-diffraction channels contribute equally, yielding $A_{s1} = A_{s2} = A_{s12} = A_{s21}$. Consequently, the signal conversion efficiency scales as $\eta_s \propto |A_s|^2 = |A_{s1} + A_{s2}|^2$, while the diffraction efficiency scales as $\eta_{diff} \propto |A_{s12}|^2 + |A_{s21}|^2$. The total efficiency saturates at the quantum limit $\omega_s/\omega_p = 64.4\%$, with η_{diff} reaching a theoretical maximum of 21.5% – one third of this limit.

Subsequently, we examine the influence of idler dissipation on parametric diffraction by simulating a two-beam-pumped QPCPA system. To evaluate the QPCPA performance, the dispersion parameters of pure YCOB without rare-earth ion doping are likewise employed, with the idler dissipation coefficient α treated as a numerically adjustable parameter. This approach isolates the specific contribution of idler absorption to the amplification process. For the following analysis, an idler dissipation coefficient of $\alpha = 40$ cm^{-1} and a crystal length of $z = 20$ mm are assumed.

Figure 3(a) illustrates that, in contrast to conventional OPCPA, the diffraction efficiency η_{diff} in a two-beam-pumped QPCPA exhibits distinct dynamics across gain regimes: while η_{diff} increases rapidly during the small-signal amplification region, it stabilizes at a minimal added value upon reaching saturation. This trend indicates the effective suppression of cross-coupling through idler dissipation. Quantitatively, at $\theta_{p1p2} = 15$ mrad, η_{diff} drops from 5.6% in the OPCPA case (Figure 2(a)) to 0.6% in the QPCPA configuration (Figure 3(a)) under identical pumping conditions.

The diffraction efficiency remains dependent on pump angular separation θ_{p1p2}, revealing an important design

https://doi.org/10.1017/hpl.2026.10200 Published online by Cambridge University Press

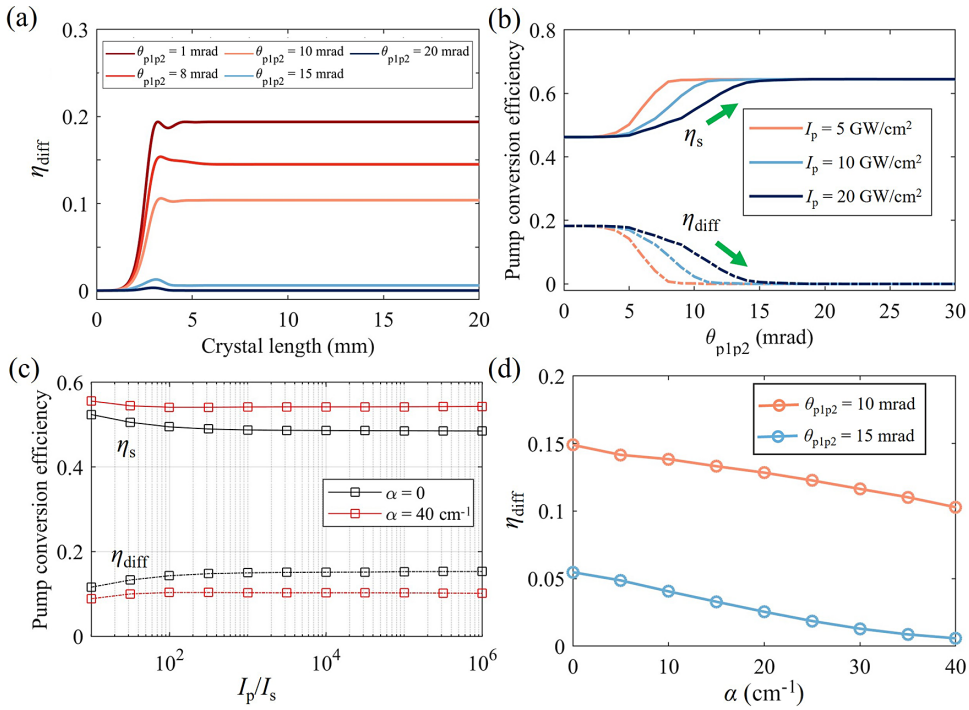


Figure 3. Parametric-diffraction characteristics in two-beam-pumped QPCPA systems. (a) Evolution of pump-to-diffraction conversion efficiency (η_{diff}) with crystal length for different pump beam separations (θ_{p1p2}), at fixed pump intensity $I_p = 20$ GW/cm^2 and idler dissipation $\alpha = 40$ cm^{-1}. (b) Angular dependence of pump conversion efficiency under the same dissipation condition ($\alpha = 40$ cm^{-1}), demonstrating critical angle thresholds for parametric-diffraction suppression. (c) Comparative analysis of pump conversion efficiencies versus pump-to-signal injection ratio (I_p/I_s) for conventional OPCPA ($\alpha = 0$) and QPCPA ($\alpha = 40$ cm^{-1}) configurations. (d) Systematic suppression of η_{diff} with increasing idler dissipation strength at $I_p = 20$ GW/cm^2, revealing an inverse scaling relation between η_{diff} and α.

trade-off. To effectively suppress parametric diffraction while maximizing signal conversion efficiency, a sufficient angular separation is required. The critical angular separation exhibits a scaling dependence on pump intensity: approximately $\theta_{p1p2} = 14$ mrad at $I_p = 20$ GW/cm^2, versus $\theta_{p1p2} = 8$ mrad at $I_p = 5$ GW/cm^2, as shown in Figure 3(b). This demonstrates the inherent trade-off between pump beam density (number of beams) and pump intensity. Stronger pump intensity requires larger angular separations, thereby reducing maximum beam packing density.

The injection ratio I_p/I_s significantly influences system performance, as illustrated in Figure 3(c). In the $I_p = 20$ GW/cm^2 and $\theta_{p1p2} = 10$ mrad case, while strong seed injection ($I_p/I_s < 10^2$) facilitates the suppression of parametric diffraction, the diffraction-induced energy loss becomes relatively insensitive to the injection ratio when $I_p/I_s \geq 10^2$.

Parametric diffraction can be directly suppressed by increasing the idler dissipation coefficient α. As shown in Figure 3(d), the steady-state diffraction efficiency η_{diff} is inversely correlated with the dissipation coefficient α. Compared to conventional OPCPA ($\alpha = 0$), at $\theta_{p1p2} = 15$ mrad, η_{diff} is reduced by 55.4% for $\alpha = 20$ cm^{-1} and by 89.3% for $\alpha = 40$ cm^{-1} in the QPCPA case. These findings confirm that enhanced idler dissipation effectively suppresses parasitic diffraction.

It is worth noting that the nonlinear phase shift of the signal induced by inter-channel crosstalk in the two-beam-pumped QPCPA configuration has been analyzed in our previous work[22]. In the present experiment, the angular separation between the two pump beams is small (7–15 mrad), leading to a negligible phase mismatch. Consequently, the associated nonlinear phase shift is minimal, and its impact on the signal's spectral phase (e.g., group delay dispersion) is expected to be insignificant under the conditions studied here.

3. Experimental comparison of two-beam-pumped optical parametric chirped-pulse amplification and quasi-parametric chirped-pulse amplification

3.1. Experimental setup

The experimental setup for the two-beam-pumped OPCPA/QPCPA system is shown in Figure 4. A single home-built ytterbium-doped yttrium aluminum garnet (Yb:YAG) laser (3 ps, 4 mJ, 100 Hz) provides both the primary pump and the seed via supercontinuum generation (SCG), ensuring passive synchronization and eliminating active timing control[31,32]. The pump laser chain consists of a

https://doi.org/10.1017/hpl.2026.10200 Published online by Cambridge University Press

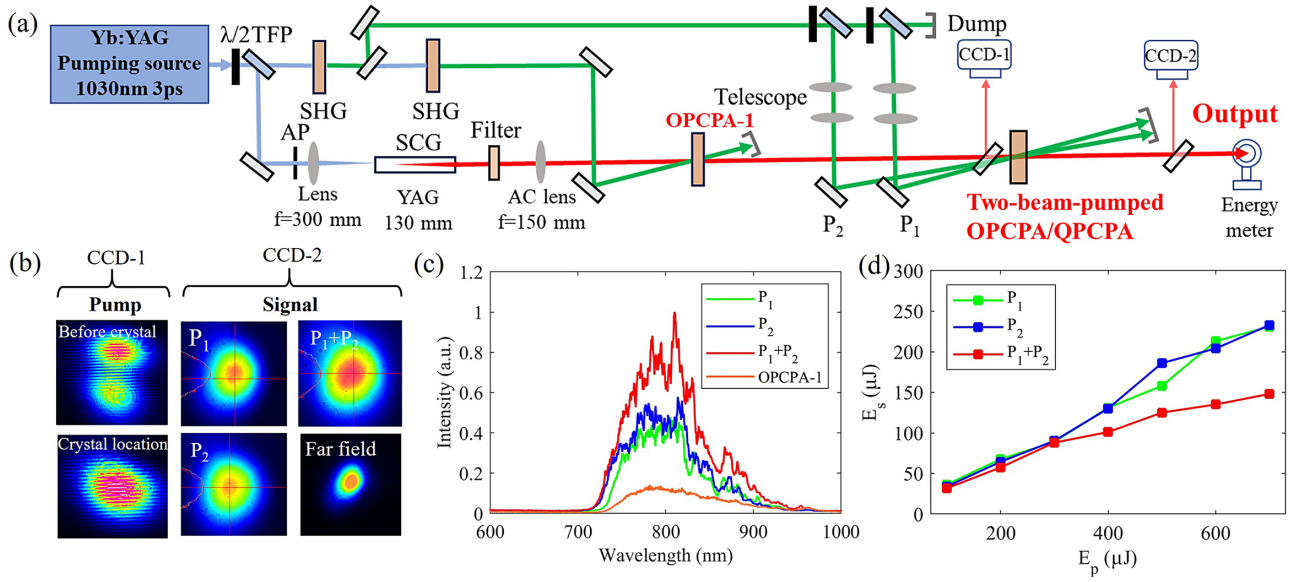


Figure 4. Experimental characterization of two-beam-pumped OPCPA/QPCPA. (a) Experimental setup. λ/2, half-wave plate; TFP, thin-film polarizer; SHG, second-harmonic generation; AP, iris aperture; SCG, supercontinuum generation; AC lens, achromatic lens. The diagnostic path includes CCD cameras for spatial profile monitoring at key positions (CCD-1 for pump characterization, CCD-2 for amplified signal analysis). (b) Measured beam profiles: the first column shows input pump beam interference patterns at CCD-1, confirming spatiotemporal overlap; the second and third columns display output signal profiles from CCD-2 for single-beam (P_1 or P_2 only) and two-beam (P_1+P_2) pumping configurations, respectively. (c) Spectral characteristics: input signal spectrum (orange curve, OPCPA-1), single-pump outputs (green and blue curves) and two-beam-pumped output (red curve). (d) Energy conversion characteristics plotting output signal energy versus total pump energy.

mode-locked fiber oscillator, a regenerative amplifier and a double-pass amplifier.

To prepare the seed, a small energy fraction (∼14 μJ) from a ps pump source is utilized for SCG. This setup employs a beam conditioning system comprising thin-film polarizers (TFPs), half-wave plates (λ/2) and an adjustable iris (AP) to enable precise control over the pulse energy and numerical aperture. Subsequently, a 300 mm plano-convex lens loosely focuses the beam into a 130 mm undoped YAG crystal. By optimizing the incident energy (considering both SCG threshold and crystal damage limits), focal position and beam parameters, we obtained a stable SCG spectrum spanning 540–950 nm with good spectral uniformity. The SCG seed is filtered via a short-pass dielectric filter with a 950 nm cutoff (Thorlabs FESH950) and collimated by a 150 mm achromatic lens (AC lens, f = 150 mm). Spectral characterization was performed using an Ocean Optics USB2000 spectrometer, and pulse energy was measured with a J-10MB-HE detector and a LabMax-TOP meter.

Regarding pump preparation, 515 nm pulses are generated via second-harmonic generation (SHG) in a 2.5 mm Type-I barium borate (BBO) crystal (θ_p = 23.4°). This process achieves a conversion efficiency of 42.8%, yielding a pump energy of 1.2 mJ. The residual 1030 nm fundamental light is further frequency-doubled to give 0.2 mJ (515 nm) for the first OPCPA stage. This initial stage utilizes a 3 mm Type-I BBO crystal (θ_p = 24.6°) in a noncollinear configuration (α_p = 2.6°), amplifying the seed pulse energy from approximately 50 nJ to 10 μJ. In the theoretical study, we used YCOB for the OPCPA baseline and Sm:YCOB for QPCPA, where these two crystals differ essentially only in the idler absorption coefficient – constituting a clean comparison. In the experiment, however, we adopted BBO for the OPCPA reference despite these differences. The primary reason is that BBO, under a walk-off-compensated noncollinear Type-I phase-matching configuration, generates strong parasitic SHG from both the signal and idler[33], making the parametric-diffraction pattern directly visible to the naked eye. This visualization capability was essential for unambiguously demonstrating the underlying cascaded nonlinear processes.

The pre-amplified pulse is then injected into the main amplifier; this stage employs two-beam pumping with independent control of each pump arm. Pump energy is balanced and adjusted using a half-wave plate and a TFP in each path. The first pump beam (P_1) and the signal (S_0) are precisely positioned within the crystal principal plane in a walk-off compensating geometry. The second pump beam (P_2) is injected with an initial angular separation θ_{p1p2} = 15 mrad relative to P_1. Temporal overlap better than 100 fs is achieved using adjustable delay lines in both pump paths. The pump beams are collimated to 0.95 mm diameter using a telescope system, while the signal beam is slightly larger than the pump beams, acting as a soft aperture.

https://doi.org/10.1017/hpl.2026.10200 Published online by Cambridge University Press

3.2. Characterization of the amplified signal

The performance of the two-beam-pumped OPCPA was evaluated through the spatial beam profiles, spectrum and energy measurements of the amplified signal. As shown in Figure 4(b), spatial beam profiles of both pump and signal beams were captured using a high-resolution charge-coupled device (CCD) camera (BeamOn U3). Distinct interference fringes were observed at the crystal plane for the two pump beams, confirming their precise spatial and temporal overlap. Nevertheless, the amplified signal retained a near-Gaussian profile in both the near- and far-field under both single- and two-beam pumping conditions. This indicates that the scheme avoids the spatial interference modulation effects commonly encountered in coherent beam combining, ensuring robust beam quality.

As illustrated in Figure 4(c), the pre-amplified signal exhibited a smooth broadband spectrum (700–950 nm, 110.8 nm bandwidth FWHM), and single-pump configurations (P_1 or P_2 alone) produced nearly identical output spectra. In the two-beam pumping architecture, the signal spectrum was amplified uniformly across the entire bandwidth without the introduction of perceptible spectral distortion.

Energy conversion efficiency was comparable (~28.7%) across the two configurations at low pump energies ($E_p < 300$ μJ), verifying proper system alignment. However, at higher pump energy ($E_p = 700$ μJ), the two-beam pumping configuration exhibited a 36.5% reduction in efficiency. This observation is consistent with the predicted onset of parametric diffraction, which redirects pump energy away from the primary signal. These results quantitatively match our theoretical predictions (Section 2.2) regarding nonlinear wave-mixing at high intensities. These experimental results provide definitive evidence of parametric diffraction's role in impairing energy extraction efficiency for multi-beam-pumped OPCPA systems.

3.3. Experimental observation of cascaded cross-couplings

The cascaded cross-coupling in two-beam-pumped OPCPA is directly visualized in Figure 5(a), which shows the beam pattern on a diffusing screen. The image includes the two pump beams (P_1, P_2), the amplified signal (S_0) and their corresponding idler waves (I_1, I_2), along with multiple higher-order diffraction spots – a signature of cascaded wave-mixing.

To enable visual detection, the two-beam-pumped OPCPA employs a noncollinear walk-off compensating Type-I phase-matching geometry in BBO. Here, the signal is injected along the plane defined by the pump wave vector and the optic axis, on the same side of the Poynting vector walk-off of the *e*-polarized pump. This configuration promotes parasitic SHG for both the signal and idler beams, a phenomenon previously observed in BBO-based OPCPA systems[33]. The amplified signal (~820 nm) appears violet (~410 nm) due to SHG, consistent with the spectral dip in Figure 4(c). Similarly, the idler (~1445 nm) generates visible SHG components that exhibit angular dispersion across the beam profile, producing a color gradient from green to red.

The underlying process begins with conventional parametric amplification:

$$P_1 - S_0 \rightarrow I_1, \quad P_2 - S_0 \rightarrow I_2. \tag{6}$$

Cross-coupling between idlers and pumps then generates first-order diffracted waves:

$$P_1 - I_2 \rightarrow S_{12}, \quad P_2 - I_1 \rightarrow S_{21}. \tag{7}$$

These diffracted waves then drive the second-order parametric diffraction via the following:

$$P_1 - S_{21} \rightarrow I_{121}, \quad P_2 - S_{12} \rightarrow I_{212}, \tag{8a}$$

$$S_{12} + I_1 \rightarrow P_{121}, \quad S_{21} + I_2 \rightarrow P_{212}. \tag{8b}$$

The cascaded nonlinear interactions further produce the third-order diffraction as described by the following:

$$P_{121} - I_2 \rightarrow S_{1212}, \quad P_{212} - I_1 \rightarrow S_{2121}, \tag{9a}$$

$$P_{121} - S_{21} \rightarrow I_{12121}, \quad P_{212} - S_{12} \rightarrow I_{21212}, \tag{9b}$$

$$S_{12} + I_{121} \rightarrow P_{12121}, \quad S_{21} + I_{212} \rightarrow P_{21212}. \tag{9c}$$

Figure 5(d) shows the calculated angular distribution of these diffraction orders based on phase-matching conditions. The excellent agreement between the measured spot positions in Figure 5(a) and the simulated angles in Figure 5(d) confirms that the observed pattern arises from phase-matched parametric diffraction rather than scattering light.

Furthermore, we characterize the dependence of parametric diffraction on key pump parameters. As the pump intensity increases from 7.5 to 13 GW/cm^2 (Figures 5(a) and 5(b)), higher-order diffraction becomes markedly more discernible, and the pump-to-diffraction conversion efficiency increases approximately twofold, from 19.8% to 35% (Figure 6(a)). This strong nonlinear scaling reflects the enhanced efficiency of parametric diffraction at elevated intensities, driven by strengthened nonlinear coupling.

Similarly, the angular separation is a critical determinant of diffraction behavior. Reducing the pump beam angular separation from 15 to 7 mrad at a constant pump intensity of 13 GW/cm^2 (Figures 5(b) and 5(c)) yields more prominent diffraction patterns and additional higher-order spots, accompanied by a 25.1% increase in diffraction efficiency (Figure 6(b)). This pronounced angular sensitivity stems from the phase-matching conditions that govern energy transfer between the interacting beams.

https://doi.org/10.1017/hpl.2026.10200 Published online by Cambridge University Press

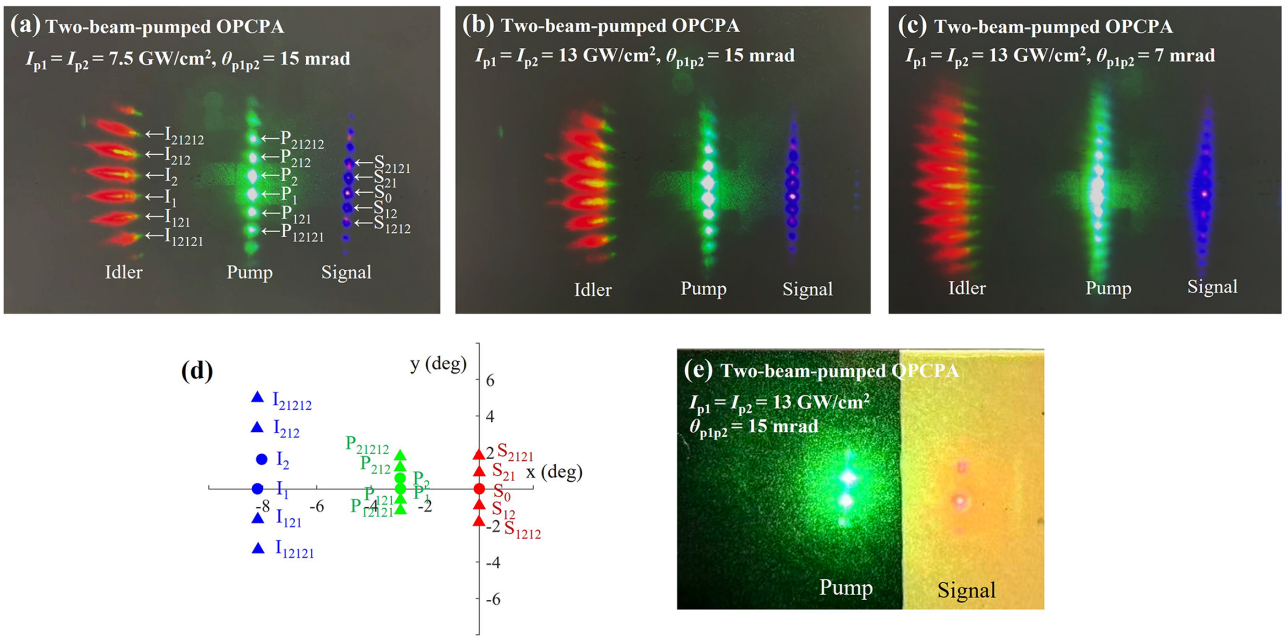


Figure 5. Experimental observation of parametric diffraction. (a)–(c) Diffraction patterns in two-beam-pumped OPCPA under different conditions: (a) at 7.5 GW/cm^2 pump intensity and 15 mrad pump beam separation; (b) at 13 GW/cm^2 (15 mrad) showing stronger diffraction; (c) at 13 GW/cm^2 with tighter 7 mrad spacing, displaying more diffraction orders. (d) Calculated angular positions of first- to third-order diffraction spots. (e) QPCPA at 13 GW/cm^2 (15 mrad) showing effective diffraction suppression. No artificial enhancement was applied to the QPCPA image; the lack of visible spots is due to the suppression of parasitic SHG.

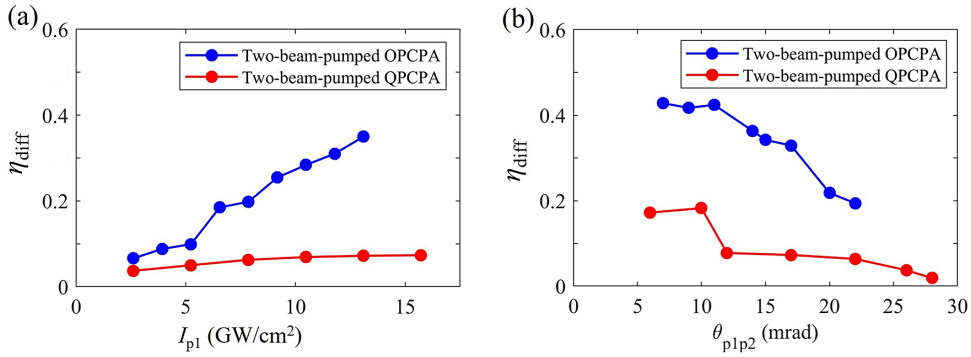


Figure 6. Experimental results of parametric-diffraction efficiency η_{diff}. (a) Measured η_{diff} versus pump intensity at 15 mrad beam angular separation. (b) Experimental angular dependence of diffraction efficiency at fixed 13 GW/cm^2 pump intensity.

3.4. Suppression of parametric diffraction via idler dissipation

For the two-beam-pumped OPCPA scheme, a 3 mm BBO crystal is used as the nonlinear medium. To implement the QPCPA configuration, we employ a 3.9-cm-long Sm:YCOB crystal with 30% Sm^{3+} doping, providing an average idler absorption coefficient of approximately 1.5 cm^{-1}[23]. It is important to note that the relevant physical parameter for the suppression mechanism is the absorption coefficient (~1.5 cm^{-1}) rather than the Sm^{3+} doping concentration (30%) itself, as the absorption depends on the specific material context. Given the peak pump intensity of approximately 13 GW/cm^2 and the nonlinear refractive index of Sm:YCOB ($n_2 \approx 3.2 \times 10^{-16}$ cm^2/W), the calculated B-integral is approximately 1 rad, well below the typical threshold for small-scale self-focusing (3 rad). Hence, no B-integral-related degradation or crystal damage was observed under our experimental conditions.

Unlike the BBO-based OPCPA, parasitic SHG in Sm:YCOB is too weak for direct visual observation of the diffracted idler and signal beams. To detect the diffracted light, we therefore used laser viewing cards to record the spatial distribution of the emitted beams. As shown in Figure 5(e), the QPCPA configuration exhibits negligible diffraction. Both the number of observable diffraction orders and their intensities are drastically reduced compared to the conventional OPCPA scheme. This suppression results from

https://doi.org/10.1017/hpl.2026.10200 Published online by Cambridge University Press

strong absorption of idler waves (1200–1600 nm) by Sm^{3+} ions, which interrupts the cascaded nonlinear processes that generate higher-order diffraction.

Quantitative analysis of the pump-to-diffraction conversion efficiency (η_{diff}) further reveals the performance improvement achieved by QPCPA. As shown in Figure 6(a), at a fixed angular separation of 15 mrad and pump intensities ranging from 2.6 to 13 GW/cm^2, the conventional OPCPA exhibits a sharp increase in η_{diff}, reaching 35% at 13 GW/cm^2. In contrast, η_{diff} for QPCPA remains stable near 7%. The angular dependence at I_p = 13 GW/cm^2 further elucidates this suppression effect (Figure 6(b)): the OPCPA shows a dramatic escalation in η_{diff} as the separation decreases, reaching 42.8% at a 7 mrad spacing, whereas the QPCPA mitigates this loss to only 17.2% under the same conditions. At larger pump angular separations (e.g., 22 mrad), the QPCPA achieves a 67.2% reduction in η_{diff} relative to the OPCPA configuration.

It should be noted that the idler dissipation coefficient in the currently available Sm:YCOB crystal is approximately 1.5 cm^{-1}, limited by the Sm doping concentration of approximately 30%. This value is significantly lower than the ideal case considered in the numerical simulations ($\alpha = 40$ cm^{-1}). Nevertheless, even at this modest dissipation level, the idler absorption mechanism is expected to effectively disrupt the cascaded nonlinear processes that drive parametric diffraction, enabling observable suppression in the subsequent experimental results.

It is also worth emphasizing that pump beam interference does not degrade the main signal beam quality due to the spatial-filtering effect of phase matching. Instead, beam-quality degradation arises primarily from the parametric-diffraction beams, which are suppressed by idler dissipation. Hence, QPCPA inherently protects both the conversion efficiency and beam profile. These results demonstrate that idler dissipation not only suppresses parametric diffraction but also provides significantly greater flexibility in system design. By maintaining low parametric-diffraction losses across a broad range of pump intensities and angular separations, the QPCPA can achieve both high efficiency and a compact geometry, effectively overcoming the fundamental trade-offs inherent in parametric diffraction in conventional multi-beam OPCPA systems.

4. Conclusion

This work presents the first experimental demonstration and quantitative characterization of parametric-diffraction suppression via controlled idler dissipation in multi-beam-pumped OPCPA systems. By systematically investigating the scaling with pump intensity and beam angular separation, we show that QPCPA reduces the pump-to-diffraction conversion efficiency from 42.8% (at a pump intensity of 13 GW/cm^2) to as low as 17.2% at a beam angular separation of 7 mrad and 8.8% at 15 mrad, corresponding to 60% and 79.4% suppression, respectively. These results validate that idler dissipation provides tunable and robust suppression of parametric diffraction, despite the modest absorption coefficient (~1.5 cm^{-1}) of the currently available Sm:YCOB crystal – far lower than the ideal 40 cm^{-1} used in simulations. The observed suppression is consistent with the scaling trend in Figure 3(d), and further improvement is expected with higher Sm doping. The amplified signal in the two-beam-pumped QPCPA configuration retains a near-Gaussian near-field profile, indicating a well-behaved spatial mode. However, the beam quality in this study was not quantified via an M^2 factor or Strehl ratio measurement; a quantitative characterization of the beam quality remains a subject for future work.

The underlying mechanism is that selective idler absorption interrupts the cascaded wave-mixing processes driving parametric diffraction, enabling stable operation at higher pump intensities and denser beam configurations. By bridging theory and experiment, this work advances QPCPA from a concept to a validated technique, offering a concrete pathway for energy scaling in multi-beam nonlinear combining architectures. Although the current study is based on a low-average-power platform, the established suppression mechanism is general and paves the way for high-repetition-rate implementations, where thermal management can be addressed through non-absorptive dissipation schemes currently under development.

Acknowledgements

This work was supported by the National Key Research and Development Program of China (Grant No. 2023YFA1608500), the National Natural Science Foundation of China (Grant No. 62575178) and the Shanghai Science and Technology Program (Grant No. 25ZR1402247).

References

1. G. M. Rossi, R. E. Mainz, Y. Yang, F. Scheiba, M. A. Silva-Toledo, S. H. Chia, P. D. Keathley, S. Fang, O. D. Mücke, C. Manzoni, G. Cerullo, G. Cirmi, and F. X. Kärtner, Nat. Photonics **14**, 629 (2020).
2. F. J. Furch, T. Witting, M. Osolodkov, F. Schel, C. P. Schulz, and M. J. J. Vrakking, J. Phys. Photonics **4**, 032001 (2022).
3. C. Maher-McWilliams, P. Douglas, and P. F. Barker, Nat. Photonics **6**, 386 (2012).
4. Y. Fu, K. Midorikawa, and E. J. Takahashi, Sci. Rep. **8**, 7692 (2018).
5. H. Fattahi, H. G. Barros, M. Gorjan, T. Nubbemeyer, B. Alsaif, C. Y. Teisset, M. Schultze, S. Prinz, M. Haefner, M. Ueffing, A. Alismail, L. Vámos, A. Schwarz, O. Pronin, J. Brons, X. T. Geng, G. Arisholm, M. Ciappina, V. S. Yakovlev, D.-E. Kim, A. M. Azzeer, N. Karpowicz, D. Sutter, Z. Major, T. Metzger, and F. Krausz, Optica **1**, 45 (2014).

https://doi.org/10.1017/hpl.2026.10200 Published online by Cambridge University Press

6. B. Wolter, M. G. Pullen, M. Baudisch, M. Sclafani, M. Hemmer, A. Senftleben, C. D. Schröter, J. Ullrich, R. Moshammer, and J. Biegert, Phys. Rev. X **5**, 021034 (2015).
7. J. D. Zuegel, S. W. Bahk, I. A. Begishev, J. Bromage, C. Dorrer, A. V. Okishev, and J. B. Oliver, in *Conference on Lasers and Electro-Optics (CLEO): Science and Innovations / Applications and Technology* (2014), paper JTh4L-4.
8. E. Cartlidge, Science **359**, 382 (2018).
9. G. Tamošauskas, A. Dubietis, G. Valiulis, and A. Piskarskas, Appl. Phys. B Lasers Opt. **91**, 305 (2008).
10. D. Kezys, M. Gecevičius, A. Piskarskas, V. Pyragaitė, V. Smilgevičius, and A. Stabinis, Lith. J. Phys. **51**, 137 (2011).
11. Y. Li, Y. Huang, J. Wang, Y. Xu, C. Wang, and Y. Leng, Opt. Commun. **289**, 131 (2013).
12. D. Herrmann, R. Tautz, F. Tavella, F. Krausz, and L. Veisz, Opt. Express **18**, 4170 (2010).
13. G. Mennerat, B. Trophème, and B. Boulanger, Opt. Lett. **38**, 3319 (2013).
14. C. Wang, Y. Leng, B. Zhao, Z. Zhang, and Z. Xu, Opt. Commun. **237**, 169 (2004).
15. Z. Rajablou and F. Jahangiri, J. Appl. Phys. **121**, 193103 (2017).
16. Z. Li and J. Kawanaka, OSA Continuum **2**, 1125 (2019).
17. Z. Li, Y. Kato, and J. Kawanaka, Sci. Rep. **11**, 151 (2021).
18. S. Ališauskas, R. Butkus, V. Pyragaitė, V. Smilgevičius, A. Stabinis, and A. Piskarskas, Opt. Commun. **283**, 469 (2010).
19. V. Pyragaite, R. Butkus, G. Archipovaitė, D. Kezys, A. Stabinis, A. Piskarskas, and V. Smilgevičius, Opt. Commun. **309**, 344 (2013).
20. D. Kezys, V. Pyragaite, A. Stabinis, R. Butkus, and V. Smilgevičius, Opt. Commun. **324**, 58 (2014).
21. A. Frolov and V. I. Trunov, Appl. Opt. **56**, 6375 (2017).
22. W. Zhu, Y. Zhang, J. Wang, J. Ma, P. Yuan, D. Zhang, H. Zhu, and L. Qian, Opt. Express **32**, 39329 (2024).
23. J. Ma, J. Wang, P. Yuan, G. Xie, K. Xiong, Y. Tu, X. Tu, E. Shi, Y. Zheng, and L. Qian, Optica **2**, 1006 (2015).
24. Y. Zhang, W. Zhu, J. Wang, J. Ma, P. Yuan, D. Zhang, H. Zhu, and L. Qian, Opt. Express **32**, 5481 (2024).
25. N. Flemens and J. Moses, Phys. Rev. Lett. **129**, 153901 (2022).
26. N. Flemens, N. Swenson, and J. Moses, Opt. Express **29**, 30590 (2021).
27. Q. Lin, J. Ma, Z. Yin, P. Yuan, J. Wang, G. Xie, and L. Qian, Fundam. Res. **4**, 43 (2024).
28. Z. Hu and J. Ma, Opt. Commun. **562**, 130556 (2024).
29. B. Trophème, B. Boulanger, and G. Mennerat, Opt. Express **20**, 26176 (2012).
30. J. Bromage, J. Rothhardt, S. Hädrich, C. Dorrer, C. Jocher, S. Demmler, J. Limpert, A. Tünnermann, and J. D. Zuegel, Opt. Express **19**, 16797 (2011).
31. L. Indra, F. Batysta, P. Hříbek, J. Novák, Z. Hubka, J. T. Green, R. Antipenkov, R. Boge, J. A. Naylon, P. Bakule, and B. Rus, Opt. Lett. **42**, 843 (2017).
32. A. Špaček, L. Indra, F. Batysta, P. Hříbek, J. T. Green, J. Novák, R. Antipenkov, P. Bakule, and B. Rus, Opt. Express **28**, 20205 (2020).
33. T. Lang, A. Harth, J. Matyschok, T. Binhammer, M. Schultze, and U. Morgner, Opt. Express **21**, 949 (2013).

https://doi.org/10.1017/hpl.2026.10200 Published online by Cambridge University Press